

Article

Bond-Damaged Prestressed AASHTO Type III Girder-Deck System with Retrofits: Parametric Study

Haoran Ni * and Riyad Aboutaha

Department of Civil and Environmental Engineering, Syracuse University, Syracuse, NY 13244, USA; rsabouta@syr.edu

* Correspondence: hni100@syr.edu

Abstract: This research describes an in-depth analysis of the flexural strength of a strengthened AASHTO Type III girder-deck system with debonding-damaged strands based on the finite element software ABAQUS 6.17. To investigate the stand-debonding impact and retrofit, two strengthening techniques by the separate use of carbon fiber-reinforced polymer (CFRP) and steel plate (SP) were proposed. A detailed finite element analysis (FEA) model considering strand debonding, material deterioration, and retrofitting systems was developed and verified against relevant experimental data obtained by other researchers. The proposed FEA model and the experimental data were in good agreement. The sensitivity of the numerical model to the mesh size, element type, dilation angle and coefficient of friction was also investigated. Based on the verified FEA model, 156 girder-deck systems were studied, considering the following variables: (1) debonding level, (2) span-to-depth ratio (L/d), (3) strengthening type, and (4) strengthening material amount. The results indicated that the debonding level and span-to-depth ratio had a major effect on both load–deflection behaviors and the ultimate strength. The relationships between the enhancement of the ultimate strength and the thickness of the strengthening material were obtained through regression equations with respect to the CFRP- and SP-strengthened specimens. The coefficient of determination (R^2) was 0.9928 for the CFRP group and 0.9968 for the SP group.

Keywords: prestressed concrete; bond damage; finite element analysis; CFRP; ABAQUS



Citation: Ni, H.; Aboutaha, R. Bond-Damaged Prestressed AASHTO Type III Girder-Deck System with Retrofits: Parametric Study. *Buildings* **2024**, *14*, 902. <https://doi.org/10.3390/buildings14040902>

Academic Editors: Atsushi Suzuki and Dinil Pushpalal

Received: 27 February 2024

Revised: 20 March 2024

Accepted: 25 March 2024

Published: 26 March 2024



Copyright: © 2024 by the authors. Licensee MDPI, Basel, Switzerland. This article is an open access article distributed under the terms and conditions of the Creative Commons Attribution (CC BY) license (<https://creativecommons.org/licenses/by/4.0/>).

1. Introduction

Prestressed concrete (PC) superstructures have been constructed in large numbers over the past several decades in the United States, particularly in the field of highway bridge girders with long spans. However, many existing highway bridges, particularly those near industrial facilities, experience large deflection issues caused by overloaded trucks or an increase in traffic density. Owing to the accumulative damage, large girder deflections and cracks result in bond reduction in the presence of an adequately large mechanical force. Over time, under frequent overloads, the bond between the strands and the surrounding concrete at critical bending sections deteriorates, which eventually results in debonding across the span section. Harries et al. [1] summarized the sources and types of observed damage for prestressed concrete girders. Almost all the cases were related to strand bonds. Strand bonds are unique interactions between prestressed steels and the surrounding concrete. Poor strand bonds cannot ensure that the strand and surrounding concrete function as a composite material with external loading [2]. FRP materials have many advantages over traditional repair materials in terms of their superior mechanical and chemical properties and easy constructability [3]. Additionally, it has been proven that bonded-steel plate strengthening is faster than other reinforcement methods and has a higher modulus of elasticity and ductility. Therefore, steel plates are considered as an effective strengthening technique.

For PC structures, many researchers [4–8] have developed bond-slip models based on the typical bond-slip relationship provided by the CEB-FIP Model Code [9]. Wang [8]

explained that the mechanism of bond failure is such that the bond strength and stiffness are the result of the adhesive force only under self-weight after strand release. When a PC member experiences an overload, the adhesive force gradually disappears. The surrounding concrete subsequently induces a friction force and mechanical interlocking force at the strand–concrete interaction. With an increase in the external overload, local crushing occurs, and the bond stress gradually decreases until strand bond slip occurs. Mohandoss et al. [10] described the bond failure mechanism by the force equilibrium at the strand–concrete interface. Researchers [11,12] demonstrated that the cracking number, width, and propagation in PC girders are affected by the debonding length and position. Girders with different bond conditions show a similar load–deflection behavior before the cracking load. Insufficient bonding results in ductility reduction. The strand debonding level also affects the cracking load and prestressing loss.

In recent decades, FEA has become a reliable tool for the nonlinear analysis of complex structures. Compared with conventional laboratory tests, FEA can save significant money on materials and labor. FEA modeling considers both geometrical and material nonlinearity, which ensures that FEA can handle complex geometries and materials and provide accurate and detailed solutions. Based on the available literature, many studies in the field of structural engineering have been conducted using FEA software. Garg et al. [13] numerically simulated the model of epoxy using cohesive elements at the concrete–CFRP interface. It was demonstrated that the proposed cohesive element was capable of capturing delamination failure. Qapo et al. [14] presented a 3D nonlinear FEM for PC girders strengthened with externally bonded CFRP. For the CFRP-to-concrete interface, the bond zone between the concrete and CFRP was modeled using eight-node plane quadrilateral interface elements, and the bond-slip model developed by Sato and Vecchio [15] was adopted for modeling the CFRP-to-concrete interface. Arab et al. [16] employed the extrusion technique to simulate the interface between strands and concrete and was modeled based on the friction surface-to-surface contact model in the software. Two friction coefficients (0.7 and 1.4) were used in the study, and the authors discussed their effects on modeling results. Kang et al. [17] numerically investigated the mechanical responses of fully bonded and unbonded post-tensioned concrete members considering the tension stiffening effect. The unbonded interface was described by frictionless tangential behavior; that is, node–surface contact. Kang and Huang [18] performed an FEA of post-tensioned concrete girders with both bonded and unbonded tendons. Three modeling methods were adopted to model the unbonded and bonded strand conditions: (1) a contact technique that reflects the actual physical strand conditions in the concrete; (2) a multiple-spring system; (3) a surface-to-surface contact formulation.

Based on the existing literature, both extrusion and embedment techniques are applicable to simulate the interface between the bonded strands and the surrounding concrete. The extrusion technique provides more details between the strand and the surrounding concrete, whereas the embedment technique is efficient in terms of the computational time. Three techniques can be employed for the contact between the unbonded strands and concrete. These are contact techniques that reflect actual physical interactions, spring systems that are more flexible in solving convergence problems, and surface-to-surface contacts with tangential and normal responses. Surface-to-surface contact is the most efficient method in terms of the computational cost.

In summary, numerical studies on strengthened PC members with debonding strands are very limited. Therefore, it is important to develop a reliable FEA model for debonding prestressed AASHTO Type III girder-deck systems using various strengthening techniques. This research contributes to structural engineering by providing an in-depth understanding of the partially debonding prestressed concrete girder-deck system with retrofitting, FEA models, sensitivity study, and parametric evaluation.

2. Cross-Section and Strengthening Systems

The prestressed girder-deck systems were designed according to the AASHTO LRFD Bridge Design Specifications [19]. The girder cross-sectional geometry followed the AASHTO Type III dimensions provided in the PCI Bridge Design Manual [20]. A 203 mm (8 in) \times 1829 mm (72 in) rectangular concrete deck was casted on top of the girder. Figure 1a shows a CFRP-strengthened section. All the simply supported girder-deck systems were prestressed with a straight-strand profile. The maximum shear reinforcement was designed in this system to prevent shear failure before flexural failure.

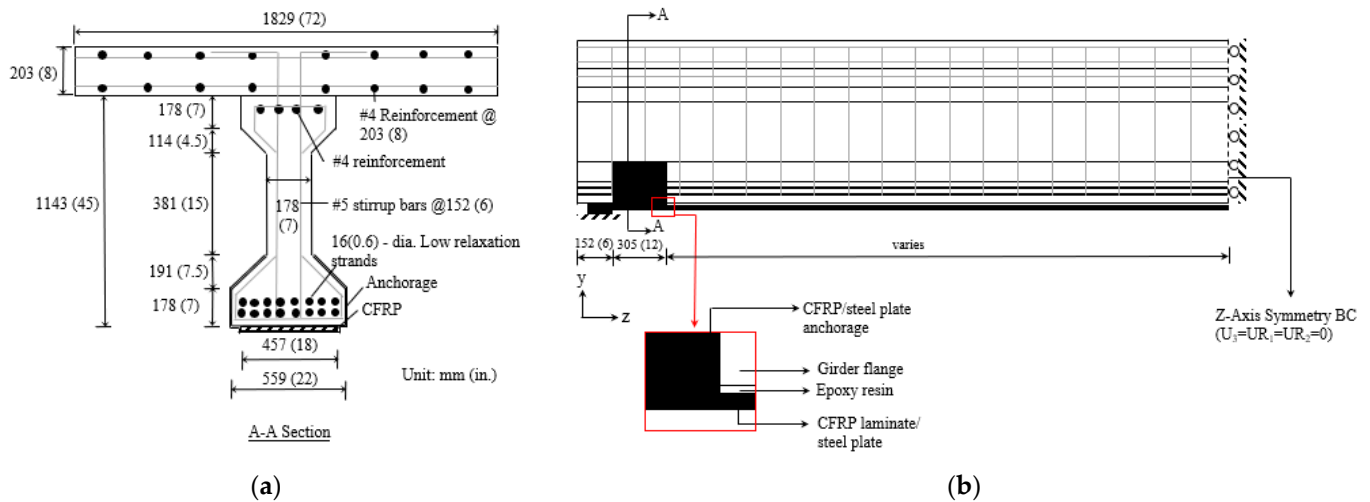


Figure 1. Details of specimens: (a) cross-sectional information; (b) strengthening systems.

Each of the girder-deck systems was reinforced with 16 Grade 270 seven-wire low-relaxation prestressing strands in the bottom flange. Each strand had a diameter of 15.2 mm (0.6 in). An effective prestressing force of 1206 Mpa (175 ksi) after prestress losses was applied to each strand. The ultimate strength of the strands adopted in the simulations was 1862 Mpa (270 ksi), the yield strength was 1675 Mpa (243 ksi), the modulus of elasticity was 198,569 Mpa (28,800 ksi), and Poisson's ratio was 0.3. In addition, US #4 Grade 60 steel was used for the non-prestressed reinforcement of both the girder and deck. Four rebars were placed on the top flange of the girder, and 16 rebars were located at both the top and bottom of the deck in the longitudinal direction. In the transverse direction of the deck, the US #4 rebars were spaced 203.2 mm (8 in) apart. To prevent shear failure before flexural failure, the maximum shear reinforcement in this system was designed with US #5 steel with a spacing of 152 mm (6 in).

Two strengthening techniques were designed to repair girder-deck systems using CFRP laminates and steel plates. For the CFRP-strengthened system, a CFRP laminate with U-shaped anchorages at both ends was externally bonded to the bottom of the concrete. The CFRP layout is shown in Figure 1b. The CFRP laminate was assumed to be perfectly bonded to the anchorage regions. A U-shaped CFRP was wrapped around the entire bottom flange with a width of 305 mm (12 in) located. Epoxy-reinforced composites with the carbon fiber volume content of 68%, a product of Sika® CarboDur® S, were employed in this study. The properties of the CFRP laminate, including the elastic behavior and the initiation and evolution criteria of damage, are described in Section 3.3. For the steel-plate-strengthened system, Grade 60 steel with the same width as that of the CFRP laminate was attached to the bottom of the concrete. Steel plates were anchored to both ends. To simplify the FEA model, the steel plate was considered to be perfectly bonded to the concrete in the anchored regions. The product Sikadur®-30, whose properties are presented in Section 3.4, was employed as epoxy resin which was used for attaching strengthening materials to the concrete. The adhesive layer thickness was 1 mm (0.04 in).

3. Material Modeling

3.1. Concrete

Concrete in compression is described as an elastic-plastic material with strain softening. The stress–strain model of concrete in compression proposed by Yang et al. [21] was employed to describe the compressive behavior of concrete, as shown in Figure 2a. Concrete stress is assumed to be elastically linear up to $0.4f'_c$, where f'_c is the ultimate concrete compressive strength. The modulus of elasticity E_c is a power law of f'_c , as expressed in Equation (1).

$$E_c = A_1 (f'_c)^a \left(\frac{w_c}{w_0} \right)^b \quad (1)$$

where $A_1 = 8470$, $a = 1/3$, and $b = 1.17$. $w_c = 2400 \text{ kg/m}^3$ (150 lb/ft³) is the concrete density and $w_0 = 2300 \text{ kg/m}^3$ (144 lb/ft³) is the reference value proposed by Yang et al. [21].

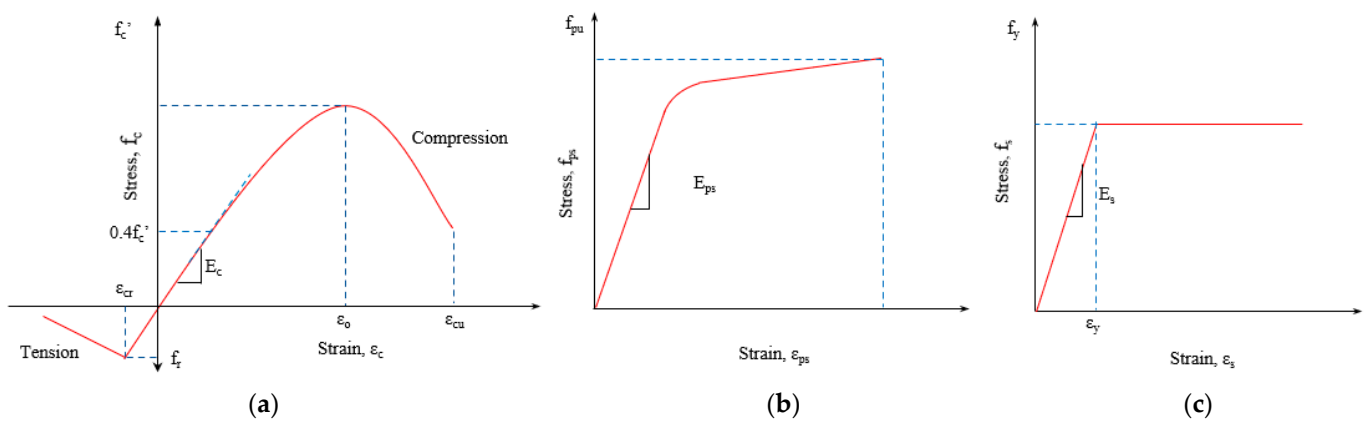


Figure 2. Constitutive relationships: (a) concrete in compression and tension [21]; (b) prestressing strand; (c) non-prestressing steel.

Above $0.4f'_c$, concrete is considered to be in a plastic stage. The calculation of the inelastic strain is shown in Equation (2). The plastic behavior of concrete consists of ascending and descending branches, given by Equation (3). In this equation, β_1 determines the slopes of the nonlinear branch. β_1 can be calculated using Equation (4) for both the ascending and descending segments.

$$\varepsilon_{in} = \varepsilon_c - \frac{f_c}{E_c} \quad (2)$$

$$f_c = \left[\frac{(\beta_1 + 1) \left(\frac{\varepsilon_c}{\varepsilon_0} \right)}{\left(\frac{\varepsilon_c}{\varepsilon_0} \right)^{\beta_1 + 1} + \beta_1} \right] f'_c \quad (3)$$

$$\beta_1 = \begin{cases} 0.2e^{0.73\zeta} & \text{for } \varepsilon_c \leq \varepsilon_0 \\ 0.41e^{0.77\zeta} & \text{for } \varepsilon_c > \varepsilon_0 \end{cases} \quad (4)$$

$$\zeta = \left(\frac{f'_c}{f_0} \right)^{0.67} \left(\frac{w_0}{w_c} \right)^{1.17} \quad (5)$$

$$\varepsilon_0 = 0.0016e^{240 \left(\frac{f'_c}{E_c} \right)} \quad (6)$$

ε_{in} is inelastic strain; ε_c and f_c are the strain and stress variables; and ζ is given by Equation (5) and used to simplify the β_1 equations. Yang et al. (2014) set f_0 and w_0 to 10 MPa (1.5 ksi) and 2300 kg/m³ (144 lb/ft³). ε_0 , expressed in Equation (6), is the strain at concrete maximum strength.

The tensile stress–strain relationship of concrete was identified using a bilinear model including the pre-cracking and post-cracking stages, as shown in Figure 2a. The first segment starts at the origin and ends at the maximum tensile strength, corresponding to the cracking strain. The second segment is characterized by a simplified linear softening branch. According to the AASHTO Bridge Design Specifications, for most regular concrete, the tensile strength can be estimated using Equation (7).

$$f_t = 0.23\sqrt{f'_c} \quad (7)$$

In this study, 10 and 20 times the cracking strain were adopted as the total strain increments in the post-cracking region for the debonding-damaged and fully bonded PC girders, respectively. The Poisson's ratio was taken as 0.2.

3.2. Prestressing Strand and Mild Steel

A 3D solid model was constructed for the strands in ABAQUS. The strands were meshed using a 6-node wedge element (C3D6). To be compatible with the points of the surrounding concrete, the cross-section of the strand was partitioned into 16 small triangles. An effective prestressing stress of 1206 MPa (175 ksi) was applied to the strands by defining a “predefined field” under a load module. The stress–strain behavior is shown in Figure 2b. Based on the PCI Design Handbook, this curve can be approximated using Equations (8) and (9). A yield strength of 1675 MPa (243 ksi) was measured at an elongation of 1%, and the approximate strain at rupture was 0.07 [20].

$$\varepsilon_{ps} \leq 0.0085 : f_{ps} = E_{ps}\varepsilon_{ps} \quad (8)$$

$$\varepsilon_{ps} > 0.0085 : f_{ps} = f_{pu} - \frac{0.04}{\varepsilon_{ps} - 0.007} \quad (9)$$

where ε_{ps} and f_{ps} are the strain and stress in strands, respectively; E_{ps} is the modulus of elasticity of strand, 198,569 MPa (28,800 ksi); and f_{pu} is the ultimate strength of the strand, 1862 MPa (270 ksi).

For mild reinforcement, the steel rebars were modeled using 2-node truss element (T3D2). A simplified bilinear elastoplastic model with a yield strength of 413 MPa (60 ksi) was employed to describe the stress–strain relationship, as shown in Figure 2c. The elastic behavior of mild steel is defined by its modulus of elasticity, E_s . Based on the ABAQUS User's Manual [22], ABAQUS approximates the smooth stress–strain behavior of a material with straight lines. Therefore, it is possible to use a straight line, which is a very close approximation of the actual material behavior, as the post-yield behavior of non-prestressed steel. The expressions for the bilinear model are given in Equations (10) and (11).

$$\varepsilon_s \leq 0.002 : f_s = E_s\varepsilon_s \quad (10)$$

$$\varepsilon_s > 0.002 : f_s = f_y \quad (11)$$

where ε_s and f_s are the strain and stress, respectively; E_s is the modulus of elasticity, 200,000 MPa (29,000 ksi); and f_y is yield strength, 413 MPa (60 ksi).

3.3. Constitutive Models for Undamaged and Damaged CFRP Laminate

Prior to damage, the CFRP laminate was modeled as a linear elastic orthotropic material with the constitutive behavior expressed in Equation (12).

$$\begin{bmatrix} \sigma_{11} \\ \sigma_{22} \\ \sigma_{33} \\ \sigma_{12} \\ \sigma_{23} \\ \sigma_{31} \end{bmatrix} = \begin{bmatrix} C_{11}^0 & C_{12}^0 & C_{13}^0 & 0 & 0 & 0 \\ C_{12}^0 & C_{22}^0 & C_{23}^0 & 0 & 0 & 0 \\ C_{13}^0 & C_{23}^0 & C_{33}^0 & 0 & 0 & 0 \\ 0 & 0 & 0 & C_{44}^0 & 0 & 0 \\ 0 & 0 & 0 & 0 & C_{55}^0 & 0 \\ 0 & 0 & 0 & 0 & 0 & C_{66}^0 \end{bmatrix} \begin{bmatrix} \varepsilon_{11} \\ \varepsilon_{22} \\ \varepsilon_{33} \\ \varepsilon_{12} \\ \varepsilon_{23} \\ \varepsilon_{31} \end{bmatrix} \quad (12)$$

where, the nine undamaged elastic constants are defined by Equations (12)–(22).

$$C_{11}^0 = E_1(1 - \nu_{23}\nu_{32})\Delta \quad (13)$$

$$C_{22}^0 = E_2(1 - \nu_{13}\nu_{31})\Delta \quad (14)$$

$$C_{33}^0 = E_3(1 - \nu_{12}\nu_{21})\Delta \quad (15)$$

$$C_{12}^0 = E_1(\nu_{21} + \nu_{31}\nu_{23})\Delta \quad (16)$$

$$C_{23}^0 = E_2(\nu_{32} + \nu_{12}\nu_{31})\Delta \quad (17)$$

$$C_{13}^0 = E_1(\nu_{31} + \nu_{21}\nu_{32})\Delta \quad (18)$$

$$C_{44}^0 = G_{12} \quad (19)$$

$$C_{55}^0 = G_{23} \quad (20)$$

$$C_{66}^0 = G_{13} \quad (21)$$

$$\Delta = 1/(1 - \nu_{12}\nu_{21} - \nu_{23}\nu_{32} - \nu_{13}\nu_{31} - 2\nu_{21}\nu_{32}\nu_{13}) \quad (22)$$

Epoxy-reinforced composites with a carbon fiber volume content of 68%, the product of Sika® CarboDur® S, were employed in this study. The main elastic parameters of CFRP followed the product data sheet of Sika® CarboDur® S, as listed in Table 1.

Table 1. Elastic properties of CFRP laminate.

E_1	E_2 (E_3)	G_{12} (G_{13})	G_{23}	ν_{12} (ν_{13})	ν_{23}
165 GPa (23,900 ksi)	11 GPa (1595 ksi)	5.3 GPa (769 ksi)	3.9 GPa (566 ksi)	0.26	0.5

Damage initiation, which is defined as the onset of material degradation at a point, is modeled on Hashin's 3D failure criterion. The damage initiation criteria consider the following four damage initiation mechanisms: fiber tension, fiber compression, matrix tension, and matrix compression, given by Equations (23)–(26).

Tensile fiber mode $\sigma_{11} \geq 0$:

$$\left(\frac{\sigma_{11}}{X_T}\right)^2 + \frac{\sigma_{12}^2 + \sigma_{13}^2}{S_{12}^2} = \begin{cases} \geq 1 & \text{failure} \\ < 1 & \text{no failure} \end{cases} \quad (23)$$

Compressive fiber mode $\sigma_{11} < 0$:

$$\left(\frac{\sigma_{11}}{X_C}\right)^2 = \begin{cases} \geq 1 & \text{failure} \\ < 1 & \text{no failure} \end{cases} \quad (24)$$

Tensile matrix mode $\sigma_{22} + \sigma_{33} \geq 0$:

$$\frac{(\sigma_{22} + \sigma_{33})^2}{Y_T^2} + \frac{\sigma_{23}^2 - \sigma_{22}\sigma_{23}}{S_{23}^2} + \frac{\sigma_{12}^2 + \sigma_{13}^2}{S_{12}^2} = \begin{cases} \geq 1 & \text{failure} \\ < 1 & \text{no failure} \end{cases} \quad (25)$$

Compressive matrix mode $\sigma_{22} + \sigma_{33} < 0$:

$$\left[\left(\frac{Y_C}{2S_{23}}\right)^2 - 1\right] \left(\frac{\sigma_{22} + \sigma_{33}}{Y_C}\right) + \frac{(\sigma_{22} + \sigma_{33})^2}{4S_{23}^2} + \frac{\sigma_{23}^2 - \sigma_{22}\sigma_{23}}{S_{23}^2} + \frac{\sigma_{12}^2 + \sigma_{13}^2}{S_{12}^2} = \begin{cases} \geq 1 & \text{failure} \\ < 1 & \text{no failure} \end{cases} \quad (26)$$

where X_T and X_C are the tensile and compressive failure strengths in the fiber direction, respectively; Y_T and Y_C are the tensile and compressive failure strengths in the y-direction (transverse to the fiber direction); and S_{ij} is the shear failure strength in the i-j plane.

The input parameters required for the Hashin damage model in ABAQUS are presented in Table 2. The CFRP laminate was meshed using an 8-node continuum shell element (SC8R) with reduced integration, hourglass control, and a finite membrane.

Table 2. Parameters of the Hashin damage model.

X_T	X_C	Y_T	Y_C	S_{12}	S_{23}
2800 MPa (406 ksi)	1654 MPa (240 ksi)	110 MPa (16 ksi)	240 MPa (35 ksi)	115 MPa (16.6 ksi)	40 MPa (5.8 ksi)

3.4. Epoxy Resin

The cohesive element COH3D8, which is widely used in modeling adhesives or bonded interfaces [23,24], was adopted to model the CFRP–concrete interface. The mechanical constitutive response of the cohesive element is defined in terms of the traction–separation law (model). The traction–separation model in ABAQUS consists of a linear elastic response followed by the initiation and evolution of damage, as seen in Figure 3. The elastic behavior in the pre-damage stage can be expressed by Equation (27), in terms of nominal stress and nominal strain.

$$\mathbf{t} = \begin{bmatrix} t_n \\ t_s \\ t_t \end{bmatrix} = \begin{bmatrix} K_{nn} & 0 & 0 \\ 0 & K_{ss} & 0 \\ 0 & 0 & K_{tt} \end{bmatrix} \begin{bmatrix} \varepsilon_n \\ \varepsilon_s \\ \varepsilon_t \end{bmatrix} = \mathbf{K}\boldsymbol{\varepsilon} \quad (27)$$

\mathbf{t} and $\boldsymbol{\varepsilon}$ are the nominal traction stress vector and nominal strain vector, respectively; \mathbf{K} is the stiffness matrix. If the cohesive layer has thickness T_c , and the stiffness and density of the adhesive material are E_c and ρ_c , respectively, the stiffness and density of the interface is given by $K_c = (E_c/T_c)$ and $\bar{\rho}_c = \rho_c T_c$, respectively. This is because the default constitutive thickness for modeling the response in terms of traction versus separation is 1.0, rather than the actual thickness of the cohesive layer. Therefore, in ABAQUS, K_c and $\bar{\rho}_c$ should be input as the material stiffness and density, respectively.

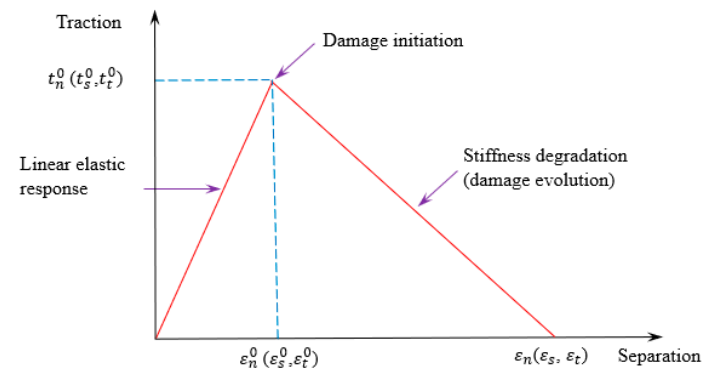


Figure 3. Typical traction–separation response [22].

The damage to the cohesive layer is assumed to be initiated if a quadratic interaction function involving the nominal stress ratios, as expressed in Equation (28), reaches unity. Once the damage initiation criterion is fulfilled, the stiffness of the cohesive material degrades according to the damage evolution law. In this study, the damage evolution was defined based on the energy conjunction with linear softening, as shown in Figure 3. The Benzeggagh–Kenane fracture criterion (Equation (29)) was used.

$$\left\{ \frac{\langle t_n \rangle}{t_n^0} \right\}^2 + \left\{ \frac{\langle t_s \rangle}{t_s^0} \right\}^2 + \left\{ \frac{\langle t_t \rangle}{t_t^0} \right\}^2 = 1 \quad (28)$$

$$G_n^C + (G_s^C - G_n^C) \left(\frac{G_S}{G_T} \right)^\eta = G_C \quad (29)$$

t_n , t_s , and t_t , respectively, are the normal and shear stresses of the cohesive material; t_n^0 , t_s^0 , and t_t^0 are the peak value of the corresponding normal and shear stresses; G_n^C and G_s^C are the critical fracture energies required to induce failure in normal and shear directions, respectively; $G_S = G_s + G_t$; $G_T = G_n + G_s$; and η is the material parameter set to 1.5.

The values of the main cohesive layer parameters, summarized in Table 3, were obtained from the product data sheet of Sikadur[®]-30, which is a high modulus, high strength, structural epoxy paste adhesive.

Table 3. Properties of cohesive material.

Elastic Properties					Damage Initiation			Damage Evolution		
E_n (GPa)	E_s (GPa)	E_t (GPa)	T_c (m)	ρ_c (kg/m ³)	t_n^0 (MPa)	t_s^0 (MPa)	t_t^0 (MPa)	G_n^C (J/m ²)	G_s^C (J/m ²)	G_t^C (J/m ²)
4.5	11.7	11.7	10 ⁻³	1650	24.8	16	16	355	280	280

4. Finite Element Modeling

4.1. Element Type, Interaction, Boundary Conditions

C3D8R was adopted considering the computational cost and shear locking. It has eight nodes and one integration point located at the center of the hexahedral brick element. A sensitivity study on the effects of different element types (C3D8, C3D8R, C3D20R) was performed, and discussed in the Sensitivity Study section. A 3D solid model was constructed for the strands in ABAQUS. The strands were meshed using a 6-node wedge element (C3D6). For mild reinforcement, the steel rebars were modeled using a 2-node truss element (T3D2). The CFRP laminate was meshed using an 8-node continuum shell element (SC8R) with reduced integration, hourglass control. The cohesive element COH3D8, which is widely used in modeling adhesives or bonded interfaces, was adopted to model the CFRP–concrete interface. The element types are summarized in Table 4.

Table 4. Summary in element type.

Part	Element Type	Description
Concrete, Steel Plate, rigid plate	C3D8R	• 8-node linear brick, reduced integration
Strands	C3D6	• 6-node linear triangular prism
Steel bars	T3D2	• 2-node linear displacement
CFRP	SC8R	• 8-node quadrilateral reduced integration
Epoxy	COH3D8	• 8-node cohesive element

The contact surface between the strands and concrete was simulated using a friction-governed model that included tangential and normal behaviors. As the transmission of shear and normal forces occurs across the contact interface, a frictional relationship exists between the contacting bodies. ABAQUS provides the classical isotropic Coulomb friction model, as shown in Figure 4, for modeling the tangential forces between the contact surfaces. The Coulomb friction model links the allowable frictional stress at the interface to the contact pressure between contacting bodies. According to the basic concept of the Coulomb friction model, the interface of two contacting bodies can carry shear stresses of a certain magnitude until they slide relative to each other, which is known as sticking. The critical transition point from sticking to sliding is determined by the coefficient of friction μ . Two methods are available in ABAQUS for defining the Coulomb friction model. The first method involves setting static and kinetic friction coefficients directly under the assumption that the friction coefficient decreases exponentially from the static status to the kinetic status. In the second method adopted in this study, the friction coefficient is

defined as a function of the equivalent slip rate and contact pressure. Thus, the friction coefficient can be set to a non-negative value. Based on the research conducted by Arab et al. [16], a friction coefficient of 1.4 is suitable for simulating the interaction between fully bonded strands and surrounding concrete. For the debonding-damaged strands, the friction coefficient was set to zero, which meant that the strands could slide freely in the debonding region.

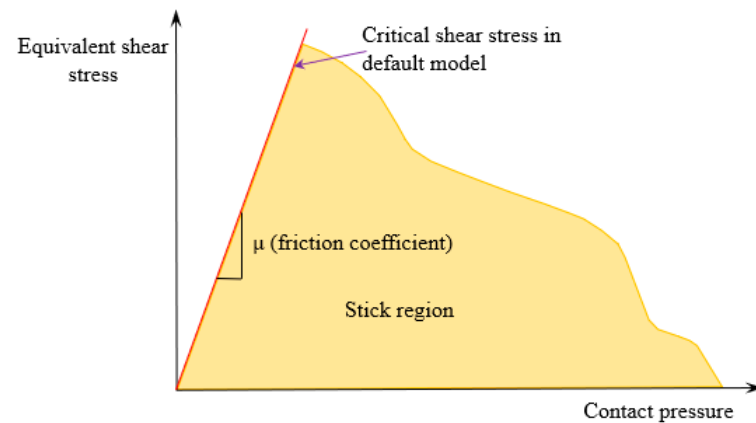


Figure 4. Basic Coulomb friction model [22].

Normal behavior was also defined to prevent strands from penetrating into surrounding concrete under overloads. The “hard” contact pressure–overclosure relationships, which can minimize the penetration of the slave surface into the master surface, were employed. In this case, the surfaces of the strands and concrete were identified as slave and master surfaces, respectively.

Owing to the doubly symmetric characteristics of the model, only a quarter of the girder-deck system was modeled considering the running time reduction, as shown in Figure 5. Using the z-direction symmetry, the girder-deck system was divided into two parts, with a plane parallel to the x-y plane. The displacement in the z-direction and rotation around the x- and y-directions were constrained by a roller support ($U_3 = UR_1 = UR_2 = 0$). Similarly, using x-direction symmetry, the girder-deck system was cut in a plane parallel to the y-z plane. The displacement in the x-direction and the rotation around the y- and z-directions were constrained by a roller support ($U_1 = UR_2 = UR_3 = 0$). In addition, the girder-deck system had a roller support that constrained the displacement in the y-direction ($U_2 = 0$) at the end.

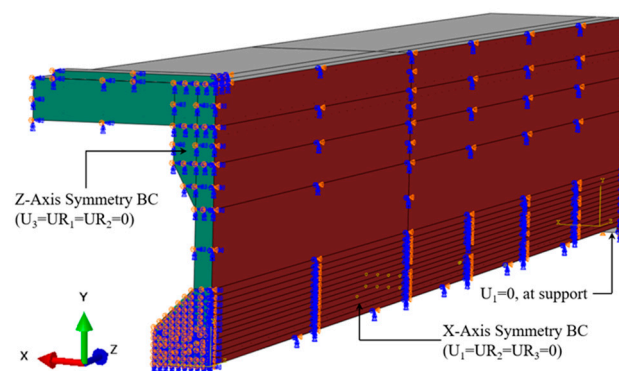


Figure 5. A quarter of a girder-deck system with BCs.

4.2. Verification of FEA Model

To validate the accuracy of the proposed FEA model, five experimental tests conducted by other researchers [25–27] were verified. These five tests included two fully bonded

prestressed concrete beams, two prestressed concrete beams with debonding strands, and one CFRP-strengthened prestressed concrete beam.

EISafty et al. [25] studied prestressed concrete girders that were laterally damaged by overheight vehicle collisions. The tested half-scale prestressed concrete girder was 20 ft long with a 4-inch-thick deck on top. Five low-relaxation-grade 270 seven-wire prestressing strands and three non-prestressed steel bars were used to reinforce the girder. The girder was loaded with four-point static loading. Ductile flexural failure was observed. The FEA model was verified using two T-section beams with debonding strands, as tested by Ozkul et al. [26]. Specimens 10 and 14 were selected for the ABAQUS model. Grade 270 (1862 MPa) seven-wire strands with a yield strength of 1689 MPa (245 ksi) were used as prestressing reinforcements. Both beams failed with concrete crushing. The two specimens tested by Meski and Harajli [27] were verified using the proposed FEA model. Beam UB2-H was used as a control beam. The other beam, UB2-H-F1 with fully debonding strands, was externally strengthened using a CFRP laminate. The thickness, modulus of elasticity, ultimate strength, and ultimate strain of the dry fibers were 0.37 mm, 230,000 MPa, 3800 MPa, and 1.7%, respectively. The corresponding values for the fiber-epoxy composites were 1.0 mm, 95,800 MPa, 986 MPa, and 1.0%. The dimensions of the CFRP laminates were 150 mm × 1.0 mm. The compressive strengths of UB2-H and UB2-H-F1 were 42 MPa (6.1 ksi) and 36 MPa (5.2 ksi), respectively. Both beams were prestressed with Grade 270 seven-wire strands. The failure mode of Specimen UB2-H was identified by concrete crushing, and the Specimen UB2-H-F1 failed with a combination of CFRP rupture and debonding.

The experimental data were compared with FEA results, and the results showed good agreement. The details of the experimental tests and the comparisons of load–deflection curves between experimental test and FEA can be found in the authors’ other paper [28]. Table 5 and Figure 6 summarize the results of the comparison between the FEA and experimental tests. It was demonstrated that the FEA model could reasonably predict the flexural response of a CFRP/steel plate-strengthened prestressed concrete girder-deck system subjected to strand-debonding damage. Based on the correlation analysis in Figure 6, the root mean squared error (RMSE) is 2.46 kips.

Table 5. Comparison between exp. and FEA data.

Scholar	Test Label	P_{cr-FEA}/P_{cr-Exp}	P_{u-FEA}/P_{u-Exp}
EISafty et al. (2012) [25]	---	1.14	1.05
Ozkul et al. (2008) [26]	No.10	1.04	1.1
	No.14	1.08	1.08
Meski and Harajli (2013) [27]	UB1-H	1	1.1
	UB1-H-F1	1.08	1.04

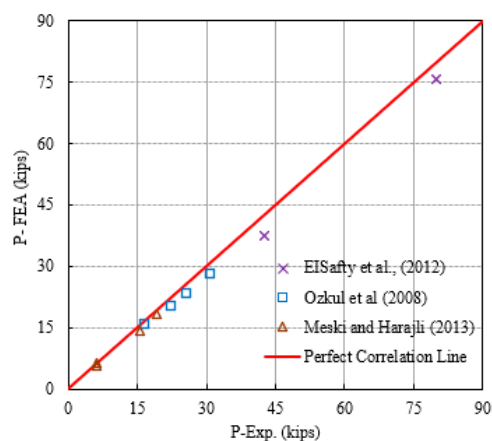


Figure 6. Comparison of the results obtained from exp. and FEA [25–27].

4.3. Sensitivity Study

The sensitivity of the numerical model was investigated regarding concrete parameters such as mesh size, element type, and dilation angle. The sensitivity of the model to the coefficient of friction between the strands and the surrounding concrete was also evaluated. The girder-deck system tested by EISafty et al. [25] was selected as the control specimen for the sensitivity analysis. The load–deflection curve, stiffness, and ultimate strength obtained from the FEA using different values of the above-mentioned parameters were compared with the data obtained from the experimental test. Figure 7 shows the results of the sensitivity study.

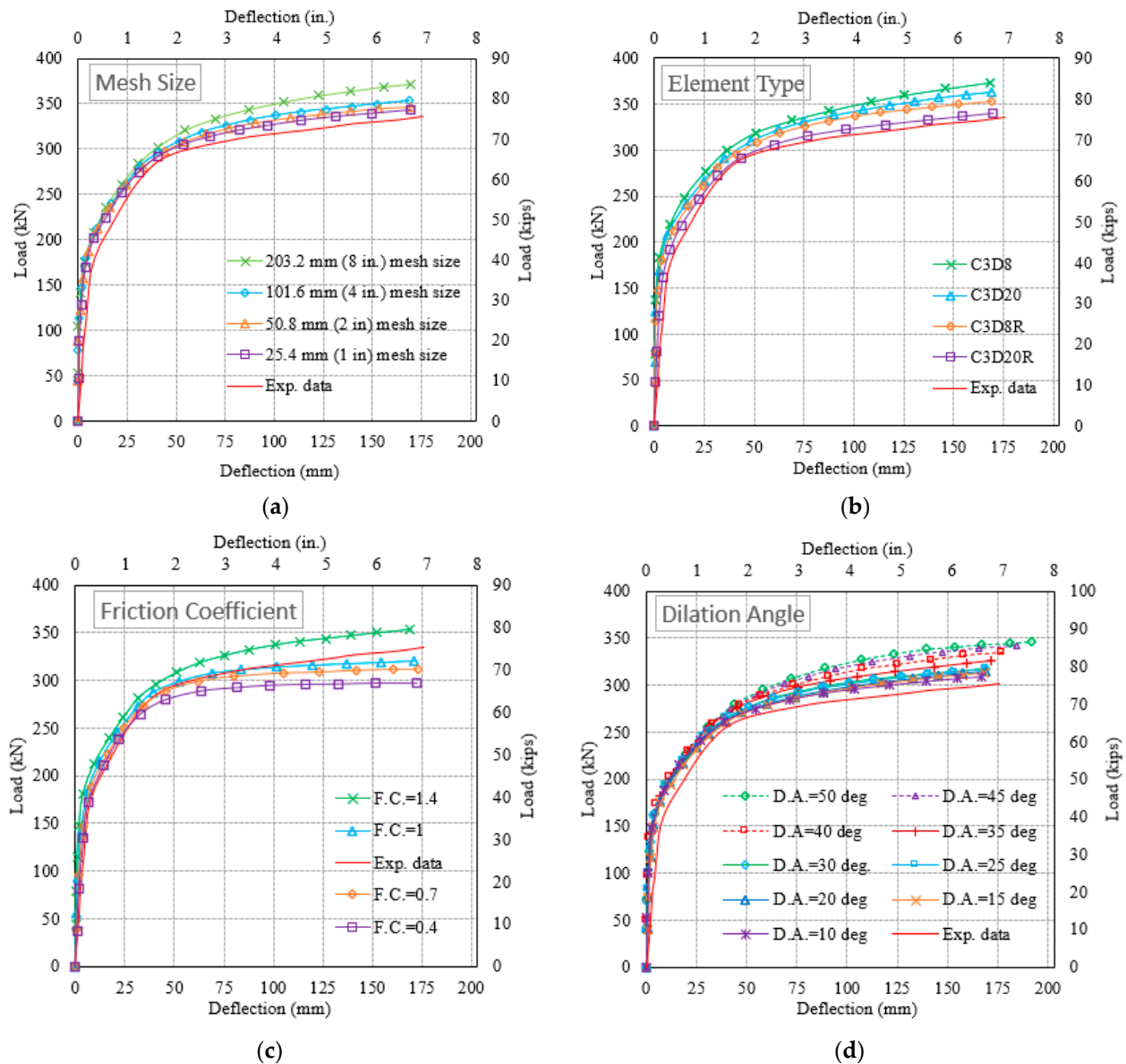


Figure 7. Sensitivity results: (a) mesh size; (b) element type; (c) friction coefficient; (d) dilation angle.

As shown in Figure 7a, a smaller mesh size produced a load–deflection curve closer to that of the experimental test. For various mesh sizes, slight differences were observed in the peak loads and deflections. The range of the differences was within the expected margin of error for numerical simulations. However, modeling with 25.4 mm (1 in) and 50.8 mm (2 in) mesh required more computational time, compared to modeling with 101.6 mm (4 in)

and 203.2 mm (8 in) mesh. Therefore, considering the time consumption and numerical accuracy, a mesh size of 101.6 mm (4 in) for concrete was employed in this study.

To investigate the effect of the element type on the simulation results, the concrete was meshed individually using four element types: standard 8-node brick element with full integration (C3D8), 8-node brick element with reduced integration (C3D8R), 20-node brick element with full integration (C3D20), and 20-node brick element with reduced integration (C3D20R). As shown in Figure 7b, the fully integrated elements (C3D8 and C3D20) were stiffer to bend compared with elements with reduced integration (C3D8R and C3D20R). This phenomenon is produced by shear locking, which occurs when shear strain develops owing to the inability of the element edges to bend. Consequently, the elements are too stiff to be used in bending-dominant problems. However, elements C3D8R and C3D20R are not sensitive to shear locking because they have fewer Gaussian integration points, and these points are closer to the element's boundaries. The load–deflection curve of C3D20R was closer to the experimental curve than that of C3D8R. This is the result of the quadratic interpolation of C3D20R. Although a quadratic interpolation element such as C3D20R can prevent shear locking and provide a more accurate bending behavior, it induces a much higher computational cost. Therefore, C3D8R was the best choice for the concrete elements in this study.

The tangential behavior at the contact surface between the bonded strands and concrete was identified by the friction coefficient. In previous studies [29,30], the friction coefficient was set to 0.4. Arab et al. [16] revealed that the friction coefficient ranges from 0.7 to 1.4 for prestressed concrete members. To study the sensitivity to the friction coefficient, FEA modeling was performed with the friction coefficient values of 0.4, 0.7, 1.0, and 1.4. As shown in Figure 7c, the friction coefficient has a negligible impact on the elastic behavior of the PC girder. The results obtained from the models with friction coefficients of 1 and 1.4 show a good match with the experimental data. For the models with friction coefficients of 0.4 and 0.7, the numerical results indicate a lower ultimate strength than the experimental values. With more simulations and verifications against other experimental data, a value of 1.4 was adopted as the friction coefficient in this study.

The dilation angle, which refers to the deviation of a concrete element subjected to shear stress, was used to determine the failure surface. One of the input parameters in ABAQUS is to define the plastic flow potential and how it governs the volumetric strain in the plastic deformation stage. The dilation angle should be greater than zero and less than 56° . Many researchers [16,30,31] used dilation angles ranging from 25° – 50° , whereas Chen and Graybeal [32] set the dilation angle to 15° . To investigate the sensitivity of the dilation angle to the flexural behavior of a concrete beam, a series of FEA were performed for ten values of the dilation angle: 10° , 15° , 20° , 25° , 30° , 35° , 40° , 45° , 50° , and 55° . As shown in Figure 7d, the dilation angle did not affect the flexural response during the elastic stage. However, the variation in the dilation angle significantly affected the post-cracking behavior. In the ultimate state, the effect of the dilation angle must be considered when it is greater than 35° . An increase in the dilation angle above 35° resulted in a higher ultimate load and corresponding deflection (Figure 8), while the computational cost decreased. No significant change in the flexural response was observed when the dilation angle was less than 35° . This variation in the effects occurs because the plastic flow potential is governed by the dilation angle and eccentricity [33]. Thus, considering the accuracy and computing time, the dilation angle was set to 30° in this study.

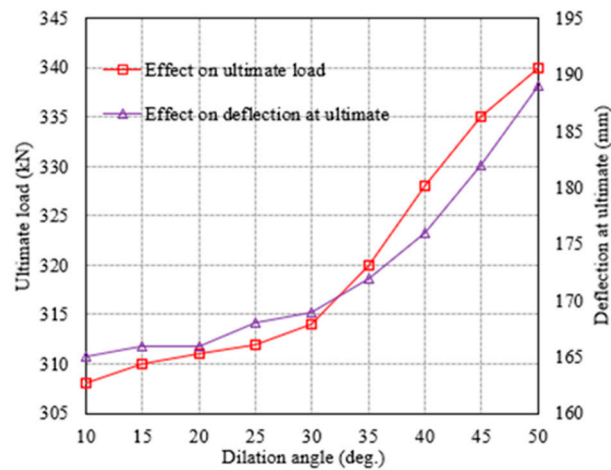


Figure 8. Effect of variation of dilation angle on ultimate load and deflection.

5. Parametric Study

5.1. Variables

Based on the FEA models presented in the previous sections, a parametric study was performed to investigate the effects of different parameters on the flexural strength of girder-deck systems. Four parameters were studied: span-to-depth ratio (10, 15, 20), debonding level (0, 20% L, 40% L, 60% L), type of strengthening material (CFRP laminate and steel plate), and amount of strengthening material ($t_{CFRP} = 0, 1, 2, 3, 4, 5$ mm for CFRP; $t_{SP} = 0, 1, 2, 3, 6, 8, 12$ mm for steel plate). The variables are summarized in Figure 9. The effects were divided into two categories: (1) un-strengthened specimens and (2) strengthened specimens. Additionally, the flexural capacity of each specimen (M_{db}) was compared with that of a fully bonded specimen (M_n) obtained from the AASHTO LRFD Bridge Design Specifications.

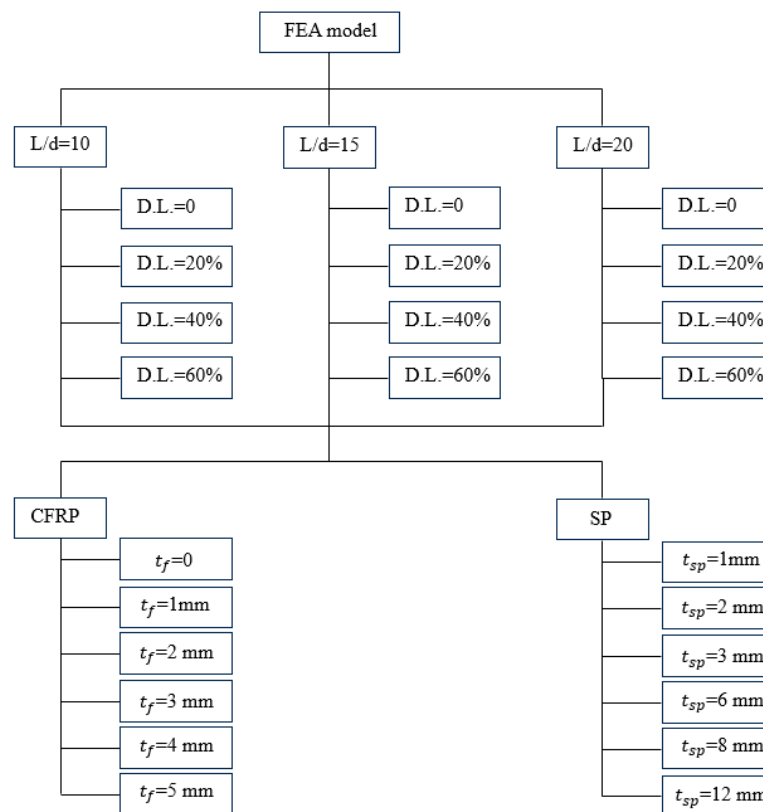


Figure 9. All cases studied by FEA model.

5.2. Modeling Process

The process to model the strengthened girder-deck system with bonded and/or debonding strands is as follows:

(1) Building the parts containing AASHTO Type III girder, concrete deck, strands, CFRP laminate, cohesive layer, steel plate, rigid support and rigid plate. (2) Applying the prestress to each strand in longitudinal direction before casting concrete by defining “PREDEFINED FIELD”. In this step, the bond properties were invalid. (3) Casting the AASHTO Type III girder and releasing the strands by applying the bond properties between the fully bonded strands and concrete. The prestressing force was transferred from the strands to the concrete using the defined bond model, and the elastic shortening was considered using ABAQUS. In this stage, only the self-weight of the girder was applied. (4) Casting the concrete deck on top of girder by activating the elements of the concrete deck in the option of “MODEL CHANGE, REACTIVATE”. (5) Applying the interface properties in the debonding region by switching the bond properties to debonding properties through the options of “CHANGE FRICTION” and “FIELD VARIABLE”. (6) Attaching the cohesive layer and strengthening materials (CFRP or steel plate). (7) Applying the overloads until failure, which was identified by concrete crushing, strand rupture, and CFRP failure. The above steps are shown in the flowchart in Figure 10.

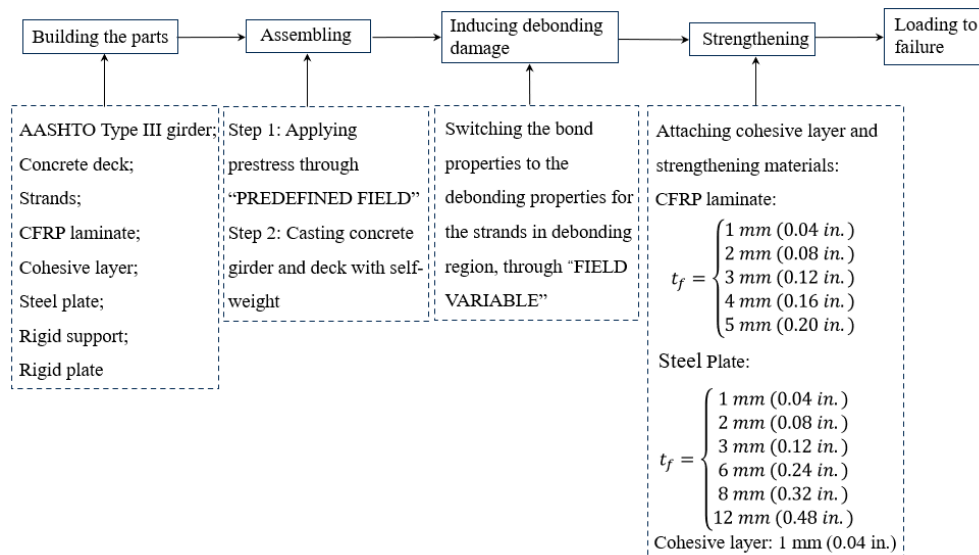


Figure 10. Modeling process.

6. Results and Discussion

6.1. Girder-Deck Systems without Strengthening

6.1.1. Effect of Debonding Level

The effects of the debonding level (λ) of un-strengthened girder-deck systems on flexural responses, including load–deflection behaviors and moment capacities, were investigated and evaluated. Figure 11 shows the load–deflection curves obtained by numerical simulations under different span-to-depth ratios ($L/d = 10, 15,$ and 20). Under the same span-to-depth ratio, the specimen with a relatively longer debonding length exhibited a lower ultimate load and higher ductility. The degree of impact of the ultimate load decreased when the span-to-depth ratio increased from 10 to 20. For both span-to-depth ratios of 10 and 15, the debonding length resulted in higher ductility than that of the control specimen with fully bonded strands. However, when the span-to-depth ratio reached 20, the ductility achieved by debonding the specimens did not exceed the ductility obtained by the control specimen. Furthermore, the stiffness was not affected by the debonding level under the same span-to-depth ratio.

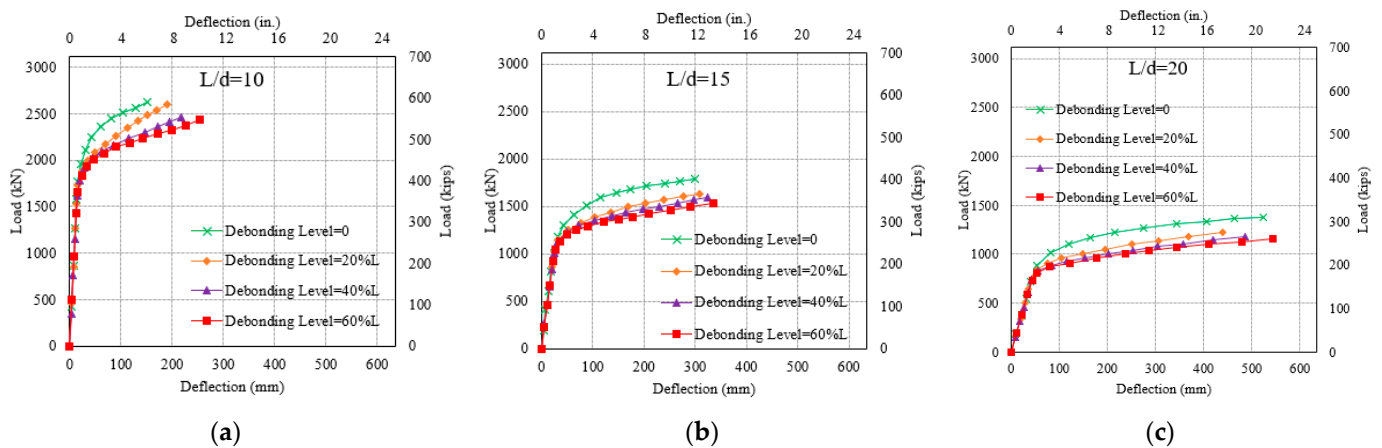


Figure 11. Load–deflection curves under the different span-to-depth ratios: (a) $L/d = 10$; (b) $L/d = 15$; (c) $L/d = 20$.

In addition to the load–deflection behaviors, the ultimate moment of the un-strengthened specimens was also evaluated. Figure 12 describes the effects of the debonding level on the ratio of M_{db} to M_n . A higher debonding level induced a lower value of M_{db}/M_n . When the debonding level changed from 20% to 40%, the ultimate moment decreased by only 1%. However, when the debonding level increased from 40% to 60%, the ultimate moment decreased by 4.5%.

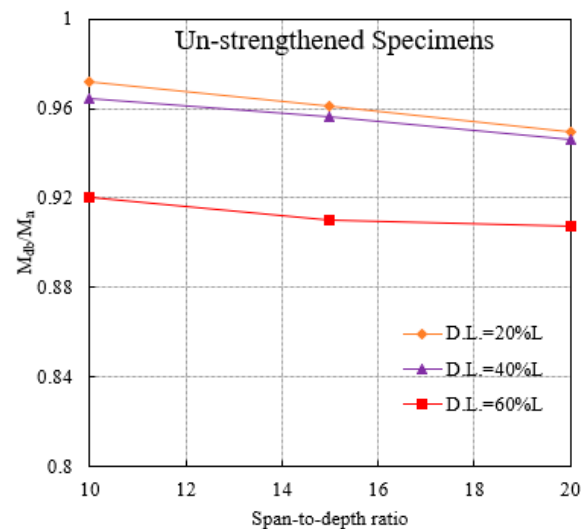


Figure 12. Effect of debonding level on M_{db}/M_n .

6.1.2. Effect of Span-to-Depth Ratio (L/d)

The effects of the span-to-depth ratio (L/d) on the load–deflection behaviors and the ultimate moment of the un-strengthened specimens with debonding strands were investigated. The debonding level of the studied specimens was 40% L and the prestressing reinforcement ratio (%) was 0.106. The load–deflection curves, shown in Figure 13a, indicate that a higher span-to-depth ratio induces a lower ultimate load and stiffness, whereas the ductility increases with an increase in the span-to-depth ratio. Figure 13b presents the influence on the ultimate moment of the un-strengthened girder deck systems with various debonding levels. The results revealed that the ultimate moment decreased with increasing span-to-depth ratio. At the same debonding level, the maximum reduction in M_{db}/M_n was 2.3% when the span-to-depth ratio increased from 10 to 20. The maximum reduction occurs at a debonding level of 20%. It is also noted that, with an increase in the debonding level, the effect of the span-to-depth ratio on the ultimate moment reduction slightly

increases. At a debonding level of 60%, the reduction in the ultimate moment was as low as 1.2%. Therefore, the effect of the span-to-depth ratio on the ultimate moment of the un-strengthened girder-deck system was negligible and can be ignored.

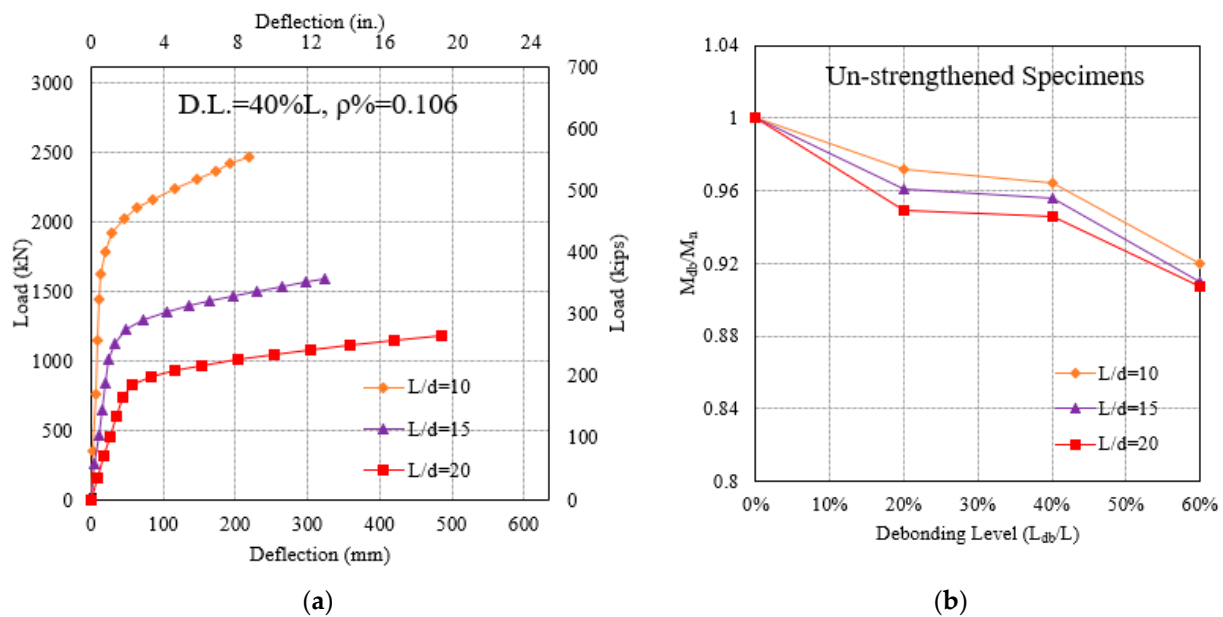


Figure 13. Effects of L/d for un-strengthened specimens: (a) on load–deflection; (b) on ultimate flexural capacity.

6.2. Girder-Deck Systems with Strengthening

6.2.1. Effect of Debonding Level

The effects of the debonding level on load–deflection behavior and the ultimate moment capacity of strengthened girder-deck systems with debonding strands were studied using two strengthening materials: CFRP laminate and SP.

Figure 14 presents the load–deflection curves of the debonding specimens strengthened using a 3 mm (0.12 in) thick CFRP laminate and SP, as an example. The specimens had a span-to-depth ratio of 15. Although the strengthening materials were different, the effect of the debonding level on the load–deflection behaviors of the strengthened specimens was similar. This indicates that a higher debonding level leads to a reduction in the ultimate load. The ultimate load decreased by approximately 5% for every 20% increment in the debonding level. The ductility increased slightly with the increase in the debonding level. The stiffness of the strengthened specimens was not affected by the debonding level, which was similar to the un-strengthened specimens.

Figure 15 shows the impact of the debonding level on the values of M_{db}/M_n for specimens with different strengthening materials: CFRP laminate and SP, respectively. The specimens had a span-to-depth ratio of 15, and were strengthened separately using CFRP laminate and SP. The thicknesses of the CFRP laminate and SP varied from 1 mm (0.04 in) to 5 mm (0.20 in), and from 1 mm (0.04 in) to 12 mm (0.48 in), respectively.

The CFRP-strengthened group, as shown in Figure 15a, indicates that the debonding level affected the ultimate moment capacity. As the debonding level increased, the ultimate moment capacity decreased considerably. However, the magnitude of this effect decreased when the debonding level increased. When the debonding level was less than 20% L , the value of M_{db}/M_n was reduced by up to 12%. When the debonding level exceeded 40% L , the maximum reduction was only 1.3%. For the specimens with thinner CFRP laminates, the debonding level significantly affected the ultimate moment capacity.

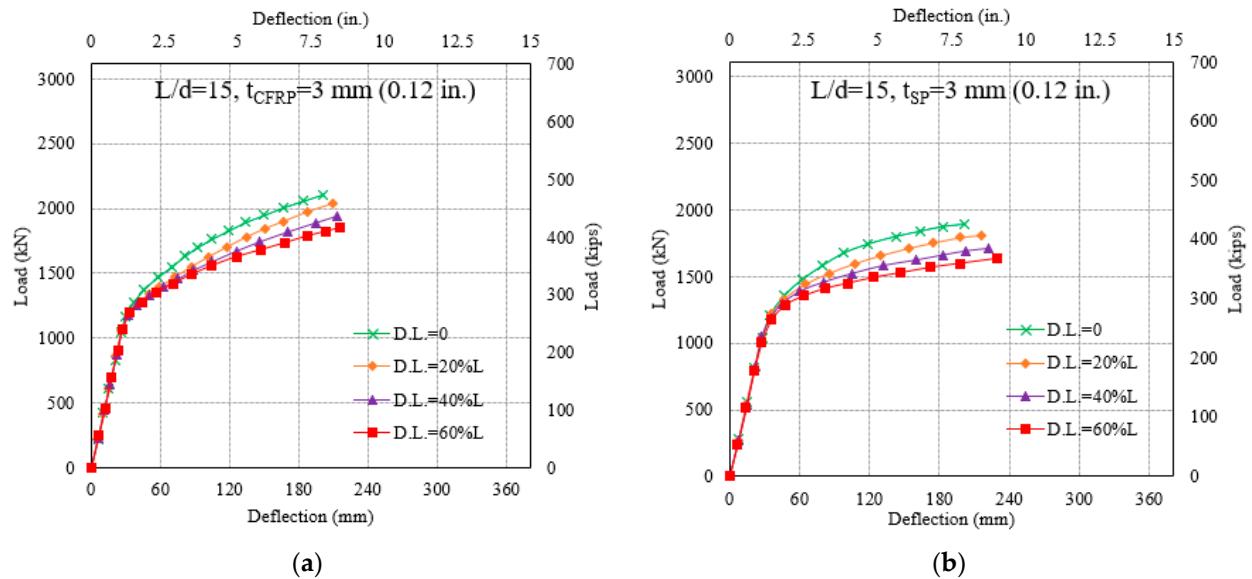


Figure 14. Load–deflection curves with various debonding levels: (a) obtained from CFRP-strengthened specimens; (b) obtained from SP-strengthened specimens.

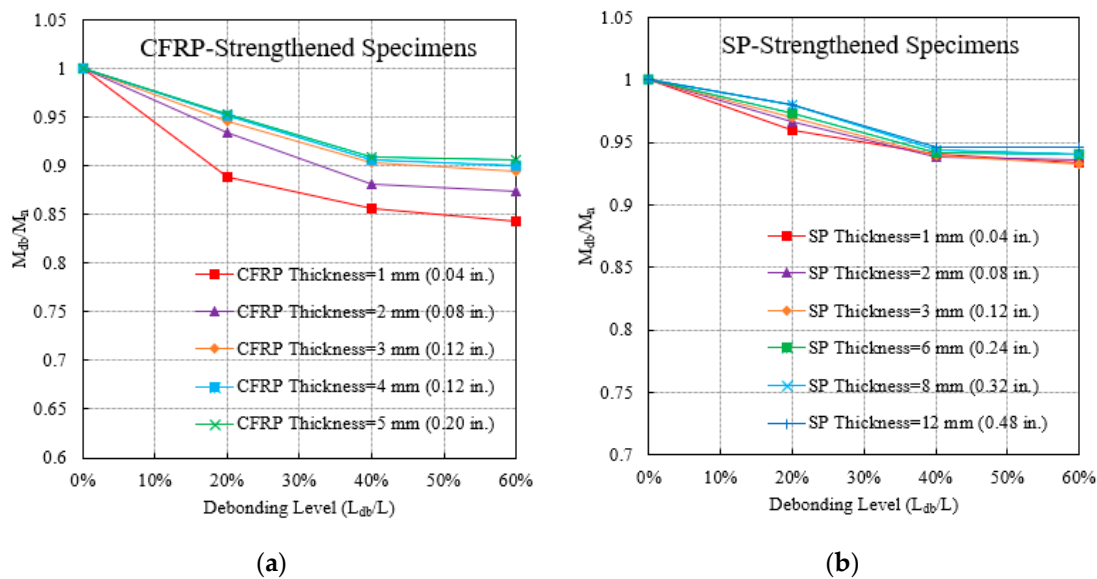


Figure 15. Effects of the debonding level on the ultimate flexural capacity: (a) for CFRP-strengthened specimens; (b) for SP-strengthened specimens.

In the SP-strengthened group, shown in Figure 15b, a higher debonding level resulted in a lower ultimate moment capacity. The percentage reduction ranged from 5.3% to 6.2% when the debonding level increased from 0 to 40%. When the debonding level exceeded 40%, the ultimate moment capacity was only slightly affected; the effect at this stage was less than 1% and can be neglected. SP thickness did not affect the degree of reduction when the debonding level increased.

6.2.2. Effect of Span-to-Depth Ratio (L/d)

The influence of the span-to-depth ratio of strengthened girder-deck systems with debonding strands on load-deflection behavior and ultimate moment capacity was studied. Specimens with a debonding level of 40% L were investigated for studying the load-deflection behavior. The specimens were separately strengthened using a 3 mm (0.12 in) CFRP laminate and SP. Figure 16a presents the load-deflection curves of the strengthened

specimens with different span-to-depth ratios ($L/d = 10, 15,$ and 20). A higher span-to-depth ratio can lower the stiffness and ultimate load for the same type and amount of strengthening material, whereas the ductility can be improved slightly.

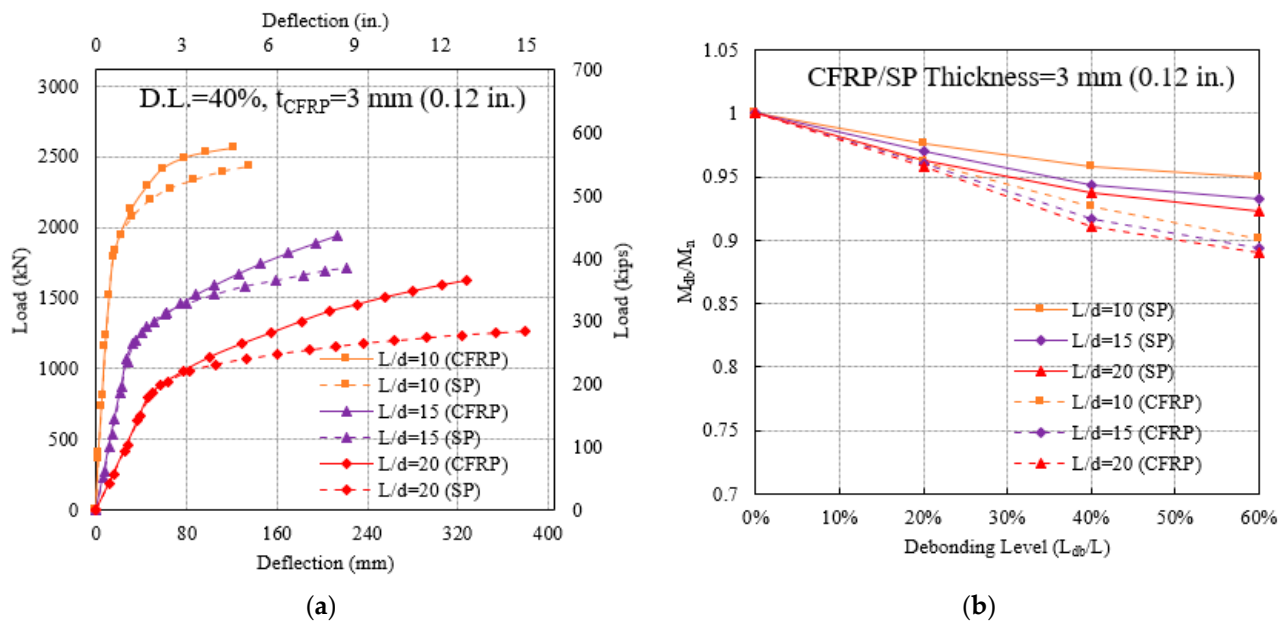


Figure 16. Effects of L/d for strengthened specimens: (a) on load–deflection; (b) on ultimate flexural capacity.

Figure 16b shows the effect of the span-to-depth ratio on the value of M_{db}/M_n , which is the ratio of the ultimate moment of the debonding specimen to that of the fully bonded (no debonding) specimen. Girder-deck systems with different debonding levels (0, 20% L , 40% L , and 60% L) and span-to-depth ratios ($L/d = 10, 15,$ and 20) were strengthened using a 3 mm (0.12 in) CFRP laminate or SP. Compared to the CFRP-strengthened specimens, the span-to-depth ratio had a relatively larger effect on the ultimate moment of the SP-strengthened specimens when the span-to-depth ratio varied from 10 to 20. In particular, the maximum reduction in the ultimate moment at the same debonding level was 3% in the SP-strengthened group when the span-to-depth ratio increased from 10 to 20. In contrast, the ultimate moment of the CFRP-strengthened specimens decreased by only 1%. Although the span-to-depth ratio had a larger effect on the SP-strengthened specimens than on the CFRP-strengthened specimens, the 3% reduction was considered negligible. In addition, the effect of the span-to-depth ratio on the ultimate moment increased with a higher debonding level. For instance, the effect of the span-to-depth ratio on the ultimate moment of the specimens with a debonding level of less than 20% L was very small. With an increase in the debonding level, the span-to-depth ratio effect increased.

6.2.3. Effect of the Type of Strengthening Material

The effects of the type of strengthening material (CFRP laminate and SP) were investigated. Figure 17 shows the enhancements in the ultimate moment of the specimens with different debonding levels (0, 20% L , 40% L , and 60% L). Half of the specimens were strengthened using a CFRP laminate with a thickness of 1 mm (0.04 in), 2 mm (0.08 in), and 3 mm (0.12 in). For comparison, the other half of the specimens was strengthened using an equal amount of SP. The CFRP- and SP-strengthened systems had the same width of 457.2 mm (18 in). For the same amount of strengthening material, the specimens strengthened using CFRP laminate can achieve much higher enhancement percentages in the ultimate moment capacity than those strengthened using SP at a certain debonding level. For instance, the ultimate moment capacity of the specimens with a 60% L debonding level improved from 15.7% to 82.5% when the thickness of the CFRP laminate varied from

1 mm (0.04 in) to 3 mm (0.12 in). However, the specimens strengthened by SP achieved an enhancement of only up to 10%. SP has a relatively lower enhancement of the ultimate moment capacity with respect to the CFRP laminate. Therefore, in this study, SP with thicker dimensions, such as 6 mm (0.24 in), 8 mm (0.24 in), and 12 mm (0.24 in), was selected. Additionally, as shown in Figure 17, the enhancement percentage increased linearly with every 1 mm (0.04 in) increment in thickness for both the CFRP laminate and SP.

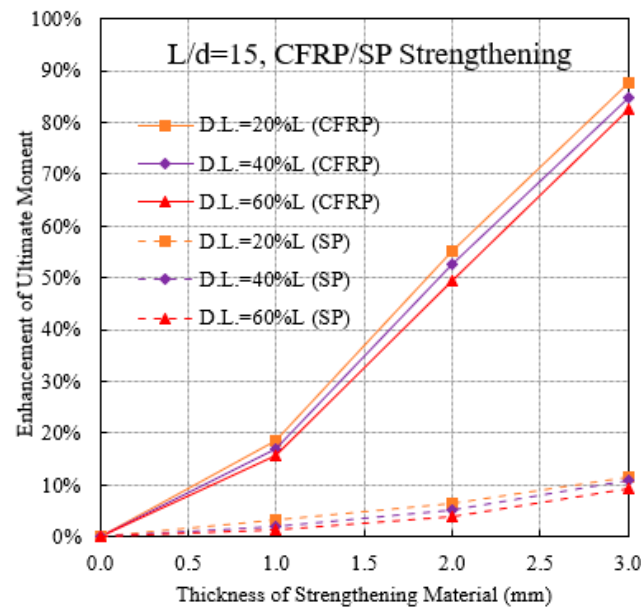


Figure 17. Enhancements on ultimate moment.

6.2.4. Effect of Amount of Strengthening Material

The effects of CFRP and/or SP amount on the ultimate load and moment capacity of the strengthened girder-deck systems with debonding strands was evaluated. Figure 18 shows the load–deflection curves of separately strengthened specimens with the span-to-depth ratio of 15 and debonding level of 60% L, and span-to-depth of 20 and debonding level of 40%, as an example in our case study. These specimens were strengthened using CFRP with thicknesses of 1 mm (0.04 in), 2 mm (0.08 in), 3 mm (0.12 in), 4 mm (0.16 in), and 5 mm (0.20 in) and using SP with thicknesses of 1 mm (0.04 in), 2 mm (0.08 in), 3 mm (0.12 in), 6 mm (0.16 in), 8 mm (0.20 in), and 12 mm (0.48 in). The specimens with higher amounts of CFRP and SP achieved a higher ultimate load than the reference specimen without any strengthening. The ultimate loads of the CFRP- and SP-strengthened specimens increased by approximately 15% and 10%, respectively. Ductility was affected by the strengthening amount. The higher the strengthening amount, the lower the ductility. The stiffness was not affected by the amount of strengthening.

The relationship between the enhancement of the ultimate moment capacity and the thickness of the strengthening material, shown in Figure 19, can be expressed using linear regression equations with respect to CFRP- and SP-strengthened specimens. The coefficients of determination (R^2) were 0.9928 and 0.9893 for the CFRP group, 0.9968 and 0.9941 for the SP group.

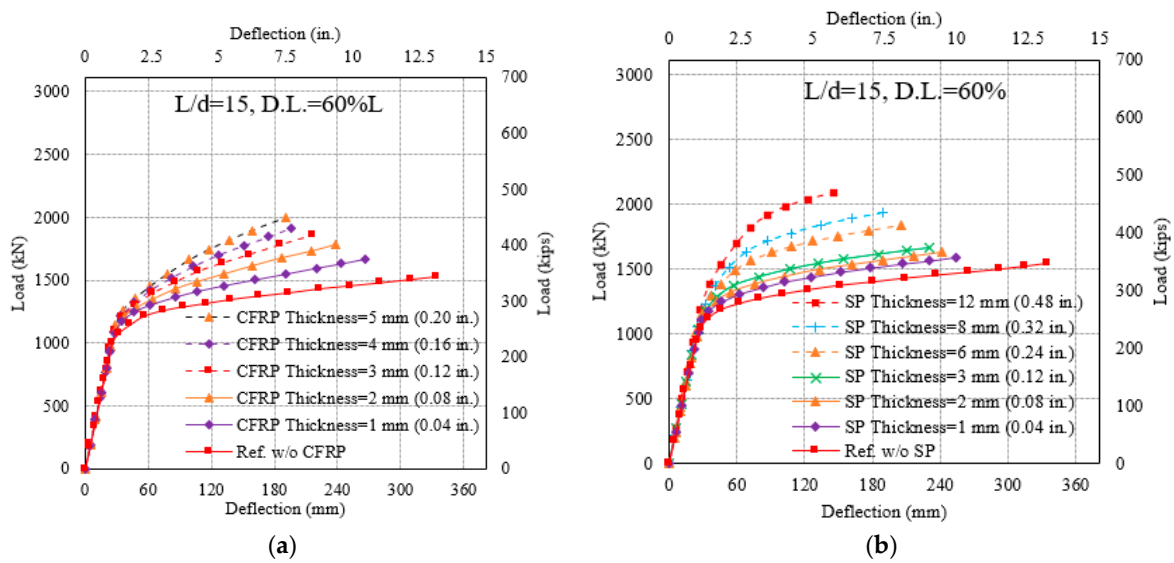


Figure 18. Load–deflection curves with various strengthening amounts: (a) obtained from CFRP-strengthened specimens; (b) obtained from SP-strengthened specimens.

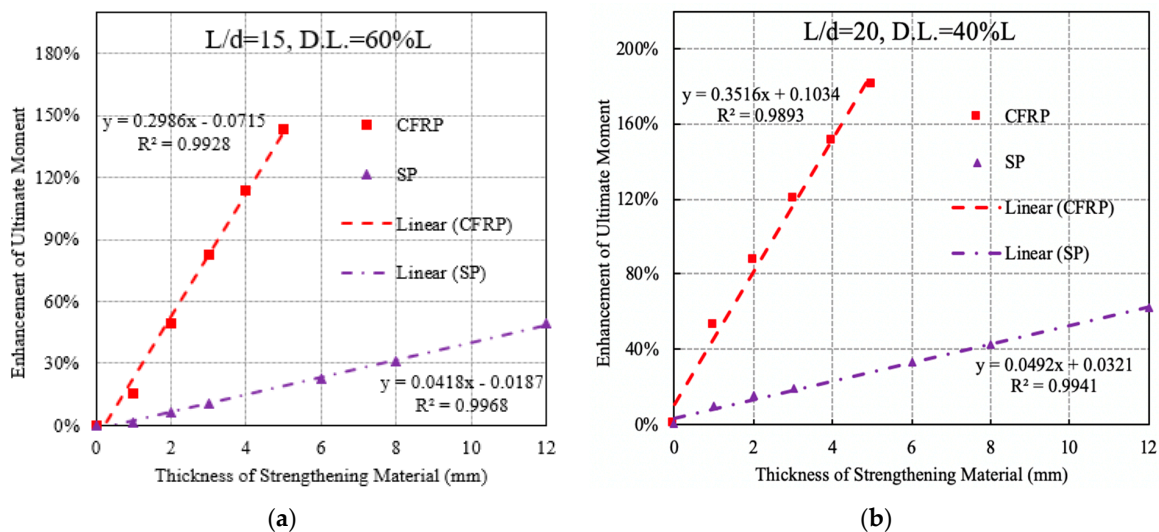


Figure 19. Relationships between ultimate moment enhancement and strengthening material thickness: (a) $L/d = 15$, $D.L. = 60\%$; (b) $L/d = 20$, $D.L. = 40\%$.

7. Summary and Conclusions

This paper presented an in-depth investigation of the flexural behaviors of CFRP- or SP-strengthened AASHTO Type III girder-deck systems with partially debonding strands based on the numerical method. A detailed FE model was proposed to predict the flexural responses of a PC member. The FE model was validated against the data from available experimental tests. The FE results were in good agreement with the experimental data by others. The FEA model was utilized to evaluate 156 strengthened and/or un-strengthened girder-deck systems with partially debonding strands. The 156 specimens included the following parameters: span-to-depth ratio, debonding level, type of strengthening material, and amount of strengthening material. A parametric study was conducted to investigate the effects of these parameters on the flexural response of girder-deck systems.

Based on the parametric study, the following conclusions could be drawn:

- Girder-deck systems without strengthening
 - (1) For the same span-to-depth ratio, the specimen with a longer debonding length achieved a lower ultimate load and higher ductility.

- (2) A higher debonding level induced a lower value of M_{db}/M_n . When the debonding level increased from 40% L to 60% L, the ultimate moment decreased by 4.5%.
 - (3) A higher span-to-depth ratio lowered the ultimate load and stiffness, whereas the ductility increased.
 - (4) The ultimate moment decreased with an increasing span-to-depth ratio. With an increase in the debonding level, the effect of the span-to-depth ratio on the ultimate moment reduction increased slightly.
- Girder-deck systems with strengthening
 - (1) A higher debonding level led to a reduction in the ultimate load of the strengthened specimens. The ductility increased slightly with an increase in the debonding level. The stiffness of the strengthened specimens was not affected by the debonding level.
 - (2) With an increase in the debonding level, the ultimate moment capacity of the CFRP-strengthened specimens decreased considerably. The degree of this effect reduces when the debonding level increases. For specimens with thinner CFRP laminates, the debonding level significantly affected the ultimate moment capacity.
 - (3) A higher debonding level resulted in a lower ultimate moment capacity of the SP-strengthened specimens. The percentage reduction ranged from 5.3% to 6.2% when the debonding level increased from 0 to 40%. Above 40%, the ultimate moment capacity was affected at a negligible 1% level.
 - (4) A higher span-to-depth ratio lowered the stiffness and ultimate load under the same type and amount of strengthening material, whereas the ductility improved slightly.
 - (5) Compared with the CFRP-strengthened specimens, the span-to-depth ratio had a larger effect on the ultimate moment of the SP-strengthened specimens when the span-to-depth ratio varied from 10 to 20. In addition, the effect of the span-to-depth ratio on the ultimate moment increased with a higher debonding level.
 - (6) For the same amount of strengthening material, the specimens strengthened by the CFRP laminate achieved a much higher increase in the ultimate moment capacity than those strengthened by SP at a certain debonding level.
 - (7) The specimens with higher amounts of CFRP or SP achieved a higher ultimate load than the reference specimen without any strengthening. The ultimate loads of the CFRP- and SP-strengthened specimens increased by approximately 15% and 10%, respectively. The higher the strengthening amount, the lower the ductility.
 - (8) The relationship between the enhancement of the ultimate moment capacity and the thickness of the strengthening material can be expressed using linear regression equations with respect to the CFRP- and SP-strengthened specimens.

Author Contributions: Conceptualization, R.A.; Methodology, H.N.; Software, H.N.; Validation, H.N.; Formal analysis, H.N.; Investigation, H.N.; Resources, R.A.; Data curation, H.N.; Writing—original draft preparation, H.N.; Writing—review and editing, H.N. and R.A.; Visualization, H.N.; Supervision, R.A.; Project administration, R.A. All authors have read and agreed to the published version of the manuscript.

Funding: This research received the support of funding and computational facilities provided by the Department of Civil and Environmental Engineering at Syracuse University.

Data Availability Statement: The data used to support the findings of this study can be accessed by emailing to the corresponding author.

Acknowledgments: The authors are truly grateful to the support provided by the Department of Civil and Environmental Engineering at Syracuse University.

Conflicts of Interest: The authors declare no conflicts of interest.

Nomenclature

The symbols used in this paper are as follows:

A_1	constant parameter
C	undamaged elastic constant
d	depth from extreme top fiber of concrete to the centroid of strands
E_c	modulus of elasticity of concrete
E_{ps}	modulus of elasticity of strand
E_s	modulus of elasticity of mild steel
f_c	concrete stress
f'_c	release concrete strength
f_0	reference value
f_{ps}	stress in strand
f_{pu}	ultimate stress of strand
f_s	stress in mild steel
f'_t	tensile strength of concrete
f_y	yield strength of mild steel
G_n^C	critical fracture energy required to induce failure in normal
G_s^C	critical fracture energies required to induce failure in shear directions
K	stiffness matrix
K_c	invariant stress ratio
L	Total span of specimen
M_n	flexural capacity of specimens
M_{db}	flexural capacity of specimens with debonding strands
P_{cr-Exp}	cracking load from experimental test
P_{cr-FEA}	cracking load from FEA model
P_{u-Exp}	ultimate load from experimental test
P_{u-FEA}	ultimate load from FEA model
t_{CFRP}	the thickness of CFRP
t_n	normal stress of the cohesive material
t_n^o	peak value of the normal stresses
t_{sp}	the thickness of steel plate
t_t	shear stresses of the cohesive material
t_t^o	peak value of the shear stresses
w_c	the density of concrete
w_0	reference density of concrete
X_C	compressive failure strength in fiber direction
X_T	tensile failure strength in fiber direction
Y_T	tensile failure strength in direction Y (transverse to fiber direction)
Y_C	compressive failure strength in direction Y (transverse to fiber direction)
η	viscosity parameter representing the relaxation time of the viscoplastic system
μ	friction coefficient
σ	reinforcement stress
σ_c	stress of concrete
λ	debonding level
ε_c	concrete strain
ε_{in}	inelastic strain
ε_{ps}	the strain in strand
ε_s	strain in mild steel
β_1	a key parameter that determines slopes of nonlinear branches of concrete constitutive model
ξ	a parameter which is used to simplify Equation (4)
ψ	dilation angle
S_{ij}	shear failure strength in i-j plane
ρ_c	density of adhesive material
Δ	a parameter which used to simplify the equation of C

References

1. Harries, K.A.; Kasan, J.; Aktas, J. *No. FHWA-PA-2009-008-PIT 006; Repair Methods for Prestressed Girder Bridges*; Department of Transportation: Harrisburg, PA, USA, 2009.
2. Dang, C.N.; Murray, C.D.; Floyd, R.W.; Hale, W.M.; Martí-Vargas, J.R. Analysis of bond stress distribution for prestressing strand by Standard Test for Strand Bond. *Eng. Struct.* **2014**, *72*, 152–159. [[CrossRef](#)]
3. Sim, J.; Park, C. Characteristics of basalt fiber as a strengthening material for concrete structures. *Compos. Part B Eng.* **2005**, *36*, 504–512. [[CrossRef](#)]
4. Haskett, M.; Oehlers, D.J.; Ali, M.M. Local and global bond characteristics of steel reinforcing bars. *Eng. Struct.* **2008**, *30*, 376–383. [[CrossRef](#)]
5. Yu, Q.; Bazant, Z.P.; Wendner, R. Improved algorithm for efficient and realistic creep analysis of large creep-sensitive concrete structures. *ACI Struct. J.* **2012**, *109*, 665. [[CrossRef](#)]
6. Xu, L.; Hai, T.K.; King, L.C. Bond stress-slip prediction under pullout and dowel action in reinforced concrete joints. *ACI Struct. J.* **2014**, *111*, 977. [[CrossRef](#)]
7. Zhang, X.; Wang, L.; Zhang, J.; Liu, Y. Model for flexural strength calculation of corroded RC beams considering bond-slip behavior. *J. Eng. Mech.* **2016**, *142*, 04016038. [[CrossRef](#)]
8. Wang, L. *Strand Corrosion in Prestressed Concrete Structures*, 1st ed.; Springer Nature: Singapore, 2023; pp. 105–135. [[CrossRef](#)]
9. Code, M. *FIB Model Code for Concrete Structures*, 1st ed.; Ernst & Sohn: Iselin, NJ, USA, 2013.
10. Mohandoss, P.; Pillai, R.G.; Gettu, R. Determining bond strength of seven-wire strands in prestressed concrete. *Structures* **2021**, *33*, 2413–2423. [[CrossRef](#)]
11. Wang, L.; Zhang, X.; Zhang, J.; Ma, Y.; Xiang, Y.; Liu, Y. Effect of insufficient grouting and strand corrosion on flexural behavior of PC beams. *Constr. Build. Mater.* **2014**, *53*, 213–224. [[CrossRef](#)]
12. Mousa, M.I.; Mahdy, M.G.; Abdel-Reheem, A.H.; Yehia, A.Z. Mechanical properties of self-curing concrete (SCUC). *HBRC J.* **2015**, *11*, 311–320. [[CrossRef](#)]
13. Garg, S.; Matsagar, V.; Marburg, S. Nonlinear finite element analyses of prestressed concrete beams strengthened with CFRP laminate. *Struct. Eng. Int.* **2023**, *33*, 258–264. [[CrossRef](#)]
14. Qapo, M.; Dirar, S.; Yang, J.; Elshafie, M.Z. Nonlinear finite element modelling and parametric study of CFRP shear-strengthened prestressed concrete girders. *Constr. Build. Mater.* **2015**, *76*, 245–255. [[CrossRef](#)]
15. Sato, Y.; Vecchio, F.J. Tension stiffening and crack formation in reinforced concrete members with fiber-reinforced polymer sheets. *J. Struct. Eng.* **2003**, *129*, 717–724. [[CrossRef](#)]
16. Arab, A.A.; Badie, S.S.; Manzari, M.T. A methodological approach for finite element modeling of pretensioned concrete members at the release of pretensioning. *Eng. Struct.* **2011**, *33*, 1918–1929. [[CrossRef](#)]
17. Kang, T.H.K.; Huang, Y.; Shin, M.; Lee, J.D.; Cho, A.S. Experimental and numerical assessment of bonded and unbonded post-tensioned concrete members. *ACI Struct. J.* **2015**, *112*, 735–748. [[CrossRef](#)]
18. Kang, T.H.K.; Huang, Y. Nonlinear finite element analyses of unbonded post-tensioned slab-column connections. *PTI J.* **2012**, *8*, 4–19.
19. American Association of State Highway and Transportation Officials (AASHTO LRFD). *AASHTO LRFD Bridge Design Specifications*, 9th ed.; AASHTO LRFD: Washington, DC, USA, 2020.
20. Precast/Prestressed Concrete Institute (PCI). *Precast and Prestressed Concrete Handbook*, 8th ed.; PCI: Chicago, IL, USA, 2020.
21. Yang, K.H.; Mun, J.H.; Cho, M.S.; Kang, T.H. Stress-strain model for various unconfined concretes in compression. *ACI Struct. J.* **2014**, *111*, 819. [[CrossRef](#)]
22. *ABAQUS User's Manual, ABAQUS 6.17*; Dassault Systèmes Simulia Corp: Providence, RI, USA, 2016.
23. Jiang, J.; Zou, Y.; Yang, J.; Zhou, J.; Zhang, Z.; Huang, Z. Study on bending performance of epoxy adhesive prefabricated UHPC-steel composite bridge deck. *Adv. Civ. Eng.* **2021**, *2021*, 6658451. [[CrossRef](#)]
24. Hu, B.; Li, Y.; Jiang, Y.T.; Tang, H.Z. Bond behavior of hybrid FRP-to-steel joints. *Compos. Struct.* **2020**, *237*, 111936. [[CrossRef](#)]
25. ElSafty, A.; Graeff, M.K.; Fallaha, S. Behavior of laterally damaged prestressed concrete bridge girders repaired with CFRP laminates under static and fatigue loading. *Int. J. Concr. Struct. Mater.* **2014**, *8*, 43–59. [[CrossRef](#)]
26. Ozkul, O.; Nassif, H.; Tanchan, P.; Harajli, M. Rational approach for predicting stress in beams with unbonded tendons. *ACI Struct. J.* **2008**, *105*, 338. [[CrossRef](#)]
27. El Meski, F.; Harajli, M. Flexural behavior of unbonded posttensioned concrete members strengthened using external FRP composites. *J. Compos. Constr.* **2013**, *17*, 197–207. [[CrossRef](#)]
28. Ni, H.; Li, R.; Aboutaha, R.S. Strengthening of prestressed girder-deck system with partially debonding strand by the use of CFRP or steel plates: Analytical investigation. *Comput. Concr.* **2023**, *31*, 34–358. [[CrossRef](#)]
29. Abdelatif, A.O.; Owen, J.S.; Hussein, M.F. Modelling the prestress transfer in pre-tensioned concrete elements. *Finite Elem. Anal. Des.* **2015**, *94*, 47–63. [[CrossRef](#)]
30. Yapar, O.; Basu, P.K.; Nordendale, N. Accurate finite element modeling of pretensioned prestressed concrete beams. *Eng. Struct.* **2015**, *101*, 163–178. [[CrossRef](#)]
31. Mercan, B. Modeling and Behavior of Prestressed Concrete Spandrel Beams. Ph.D. Thesis, University of Minnesota, Minnesota, MN, USA, 2011.

32. Chen, L.; Graybeal, B.A. Modeling structural performance of ultrahigh performance concrete I-Girders. *J. Bridge Eng.* **2012**, *17*, 754–764. [[CrossRef](#)]
33. Wosatko, A.; Winnicki, A.; Polak, M.A.; Pamin, J. Role of dilatancy angle in plasticity-based models of concrete. *Arch. Civ. Mech. Eng.* **2019**, *19*, 1268–1283. [[CrossRef](#)]

Disclaimer/Publisher’s Note: The statements, opinions and data contained in all publications are solely those of the individual author(s) and contributor(s) and not of MDPI and/or the editor(s). MDPI and/or the editor(s) disclaim responsibility for any injury to people or property resulting from any ideas, methods, instructions or products referred to in the content.